Nano Research

Open Access

Research Article

Ultra-low potential formaldehyde electrooxidation to formate and H_2 on an Ag/Ag_2O heterostructure catalyst

Haitao Shi[1,§], Rui Zhang[1,§], Chongchong Wang[1], Xiaoping Kong[1], Linlin Pan[1], Meijie Wei[1], Wei Wang[1]✉, Weixin Lv[1]✉, and Lei Wang[2]✉

[1] *School of Chemistry and Chemical Engineering, Yancheng Institute of Technology, Yancheng 224051, China*
[2] *Key Laboratory of Functional Inorganic Material Chemistry, Ministry of Education of the People's Republic of China, Heilongjiang University, Harbin 150080, China*
[§] *Haitao Shi and Rui Zhang contributed equally to this work.*

Cite this article: *Nano Research*, **2025**, *18*, 94907110. https://doi.org/10.26599/NR.2025.94907110

ABSTRACT: Formaldehyde oxidation reaction (FOR) is a promising reaction alternative to the anodic oxygen evolution reaction (OER) owing to its ultra-low electrolysis potential and ability to produce formate and hydrogen gas. In this work, the electrode for FOR is prepared using Ag/Ag_2O nanoparticles (Ag/Ag_2O NPs) covered with Nafion membrane as the catalysts modified onto nickel foam (NF). Ag/Ag_2O NPs@NF exhibits significantly higher FOR activity than Ag NPs@NF and Ag_2O NPs@NF. At 100 $mA \cdot cm^{-2}$, the FOR potential on the Ag/Ag_2O NPs@NF electrode is only 0.16 V (vs. RHE). Meanwhile, the Faradaic efficiencies can reach up to 100% for both formate and H_2 produced by FOR. Density functional theory (DFT) calculations indicate that the Ag/Ag_2O heterostructure exhibits lower reaction energy barriers for generating formate and H_2 than pure Ag and Ag_2O. This work introduces a new synthetic approach for developing novel FOR catalysts and offers insights into the potential application prospects of FOR.

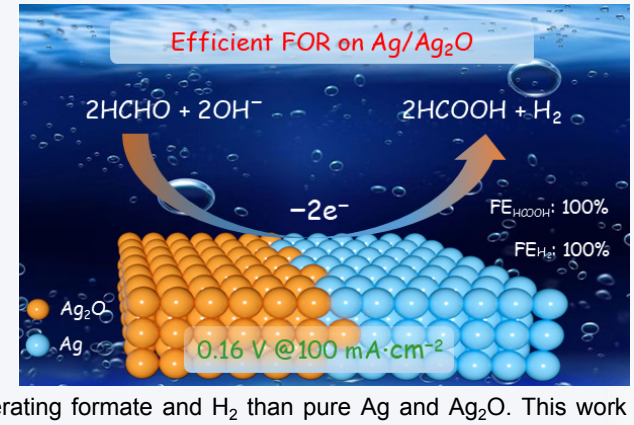

KEYWORDS: formaldehyde oxidation, ultra-low potential, heterostructure, 200% hydrogenation, formate production

1 Instruction

In recent years, there has been a significant increase in the development of energy electrocatalysis. Among these, H_2 production through water splitting has received considerable attention [1, 2]. H_2 evolution reaction (HER) is a cathodic reaction needing an effective anodic reaction to couple. The oxygen evolution reaction (OER) is the conventional anodic reaction that couples with the above-mentioned cathodic reaction. However, the high overpotential of OER leads to high power consumption for H_2 production, while on the other hand, a concern arises when the generated O_2 and H_2 mix together [3].

Although, extensive research has been reported on highly active OER catalysts [4–7]. However, water splitting's theoretical decomposition voltage (1.23 V) requires a large cell voltage input and, consequently high-energy consumption. O_2 is produced at the anode as a low-value product while H_2 is only produced at the cathode. Replacing OER with lower energy input reactions has received widespread attention in recent years. For practical applications, it is more desirable to obtain value-added products at the anode simultaneously, rather than O_2. Organic oxidation reaction (OOR) coupled with HER becomes a promising research direction for this purpose [8–12]. At the same time, value-added products could be simultaneously obtained at the anode instead of O_2. Several electrocatalytic systems have been reported to couple the oxidative valorization of various chemicals (e.g., 5-hydroxymethylfurfural, furfural, urea, glucose, methanol, ethanol, ethylene glycol, formaldehyde, glycerol, xylose, hydrazine, etc.) with HER in aqueous medium [8, 13–23]. The formaldehyde oxidation reaction (FOR) can occur at extremely low potentials among these reactions. The advantages and disadvantages of the three anodic reactions mentioned above are illustrated in Fig. 1. When FOR is coupled with HER, it is possible to eliminate toxic formaldehyde

Received: July 12, 2024; **Revised:** October 7, 2024
Accepted: November 1, 2024

✉Address correspondence to Wei Wang, wangw@ycit.edu.cn; Weixin Lv, lvweixin@ycit.edu.cn; Lei Wang, wanglei0525@hlju.edu.cn

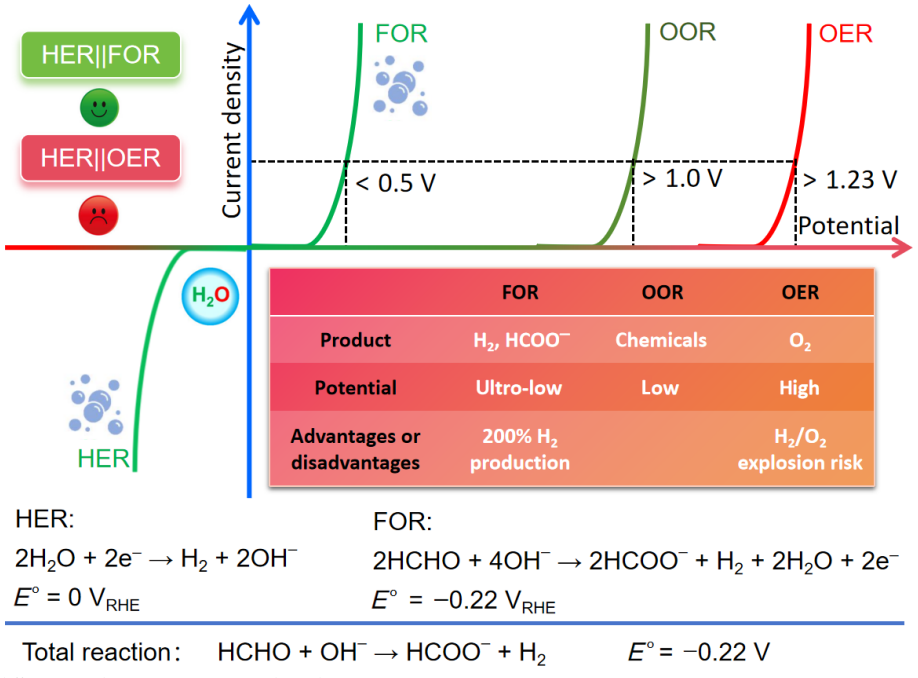

Figure 1 Comparison of different anodic reactions in water electrolysis.

residues in wastewater pollutants in addition to the production of H_2 and formate products. Coupling FOR with HER for H_2 production could also provide environmental benefits if toxic formaldehyde residues in wastewater pollutants are utilized as feedstock.

So far, some researchers have also conducted research on ultra-low potential FOR. These studies demonstrate that FOR can achieve ultra-low potential H_2 production coupled with HER leading to promising application prospects [24–29]. It is difficult for Pt or Pd with strong hydrogen oxidation ability to release H_2 as FOR catalysts. Choosing Cu or Ag with weak hydrogen oxidation ability as FOR catalysts is more conducive to releasing H_2 [13]. Li et al. synthesized Cu_3Ag_7 electrocatalyst through electrodeposition as a FOR catalyst. The required potential for FOR was only 0.1 V (vs. RHE) at 100 mA·cm^{-2} on Cu_3Ag_7, and the Faradaic efficiencies for the production of both formate and H_2 reached 100% [20]. The FOR performance of Cu_3Ag_7 is higher than those of metallic Ag and Cu, and theoretical computations indicate that Cu_3Ag_7 has stronger adsorption energy for the FOR intermediates than Ag and Cu [20]. Structural regulation of Cu or Ag based catalysts may be a solution to obtain highly active FOR catalysts. Pan et al. reported that using Cu_xO@CF electrocatalysts can catalyze FOR with high current density of 165 mA·cm^{-2} at 0.35 V (vs. RHE), their research manifesting that Cu^0 and Cu^+ are necessary and synergistic to FOR [28]. The construction of M^0 and M^+ composite catalysts is of great significance for studying the highly active FOR mechanism of this unique heterostructure.

The activity of metallic Ag as a FOR catalyst is low. Studying the Ag^0 and Ag^+ composite catalysts for FOR may promote the development of Ag-based catalysts and provide support for FOR mechanism research. So far, there have been no reports of Ag-oxide as a FOR catalyst. Ag-oxide can be easily reduced to Ag at the potential interval of FOR process, making it challenging for Ag-oxide to persist steadily. It is reported that although the potentials are past the standard reduction potentials for the metal oxides, metastable metal oxides are known to persist on electrode surfaces during cathodic reactions [30–33]. Ag-based catalysts with metastable Ag-oxide layers may be created by reducing Ag-oxide at a reducing potential. Herein, Ag/Ag_2O nanoparticles (Ag/Ag_2O NPs) catalysts covered with Nafion membrane on nickel foam (NF) was obtained by reorganizing the structure of Ag_2O NPs@NF electrode at a potential of 0.2 V for 10 min during the FOR. The FOR potential by Ag/Ag_2O NPs@NF was only 0.16 V (vs. RHE) at 100 mA·cm^{-2}, surpassing the Ag@NF and Ag_2O@NF electrodes. The Ag/Ag_2O NPs@NF exhibits 100% Faradaic efficiency (FE) to drive FOR to produce formate and H_2. By combining FOR with HER, it is possible to achieve 200% H_2 production and 100% formate production at ultra-low voltage. Furthermore, the Ag/Ag_2O NPs@NF can maintain good stability and is therefore expected to be utilized in industrial applications. The density functional theory (DFT) calculation results demonstrate that the adsorption energy of H* and $H_2C(OH)O$* on the Ag–Ag_2O interface is stronger than that of the Ag and Ag_2O surfaces. This study explains the active origin of FOR through DFT and provides theoretical guidance for the design of highly active Ag-based electrocatalysts, introducing an innovative approach for reducing the cost of electrolytic H_2 production.

2 Experimental

2.1 Preparation of Ag/Ag_2O NPs@NF and other catalysts

The NF measuring 1 × 1.3 cm was sequentially sonicated in each of HCl (3 M), anhydrous ethanol, and deionized water for 10 min, followed by gentle washing. 344 mg of $AgNO_3$ (100 mM) and 106 mg of Na_2CO_3 (50 mM) were dissolved in separate beakers. The Na_2CO_3 solution was added and vigorously stirred in a round bottom flask, followed by the rapid addition of $AgNO_3$ solution into the vortex of sodium carbonate. The reaction continued for 12 h at 30 °C. The resulting product was washed twice with distilled water and ethanol by centrifugation and subsequently dried for 6 h at 60 °C to obtain Ag_2CO_3 particles.

The Ag_2O nanospheres were obtained by annealing Ag_2CO_3 particles at 200 °C in a muffle furnace for 2 h. 20 mg of Ag_2O nanospheres were dispersed in 100 μL ethanol and 100 μL deionized water by sonication for 20 min, followed by addition of 100 μL of 5% Nafion solution and further sonication for 10 min. The dispersed solution was deposited three times onto the pre-treated NF using a 100 μL pipette and allowed to air dry. The Ag/Ag_2O NPs@NF catalyst was obtained in 1.0 M KOH with 0.6 M HCHO after 10 min electrolysis.

For preparing Ag NPs@NF, Ag_2O NPs were annealed at 200 °C for 30 min in H_2/N_2 (v_{H_2}:v_{N_2} = 1:9) environment with a flow rate of 100 mL·min^{-1}. The Ag NPs were then dispersed into 100 μL ethanol and 100 μL deionized water with 100 μL of 5% Nafion solution. Following the sonication, the suspension was dropped onto the pretreated NF. Ag plate and NF can be used as working electrodes directly following the ultrasonic treatment for 10 min with HCl (3 M), ethanol, and deionized water, respectively.

2.2 Electrochemical measurement

Electrochemical measurements were conducted in a traditional three-electrodes system with a Pt plate as the counter electrode and a Hg/HgO electrode as the reference electrode (pH = 13.8) using a CHI 760E electrochemical workstation. The electrolyte was 1.0 M KOH with 0.6 M HCHO, while Ag/Ag_2O NPs@NF, Ag NPs@NF, Ag plate, and NF, with an effective area of 1 cm × 1 cm were used as the working electrode. All potentials (V) reported in this article were calibrated with reversible hydrogen electrode (RHE) using the relation (0.098 + 0.059 × pH) V. A linear sweep voltammetry (LSV) curve was recorded at the scan rate of 5 mV·s^{-1} with 95% *iR* compensation. Electrochemical impedance spectroscopy (EIS) was performed at 0.21 V, with a frequency range of 10–10^5 Hz.

2.3 Material characterization

The morphology and structure of the catalyst were studied using various characterization techniques including scanning electron microscopy (SEM, Hitachi SU8100), Raman scattering spectrometer (Raman, HORIBA HR Evolution), powder X-ray diffraction (XRD, SmartLab), transmission electron microscopy (TEM, JEM2100F), and X-ray photoelectron spectroscopy (XPS, ESCALAB 250Xi).

2.4 Product analysis

Gas product volume was determined by drainage method. Gas product of FOR is quantitatively analyzed by gas chromatography (GC) equipped with a thermal conductivity detector and flame ionization detector, and N_2 was used as the carrier gas. The ^{1}H nuclear magnetic resonance (^{1}H NMR) spectroscope was employed to evaluate the liquid products from FOR. 72 μL of reaction electrolyte was collected, followed by the addition of 8 μL of HCl (12.0 M) for acidification, and 10 μL of t-butanol (10.0 mM) as an internal standard. Finally, 510 μL of D_2O was added. The standard curve for formate was obtained using different concentrations of sodium formate aqueous solution.

The Faradaic efficiency (FE) of formate or H_2 was calculated using the following equation (Eq. (1))

$$\mathrm{FE} = \frac{(\text{mole of formed product}) \times n \times F}{Q} \times 100\% \quad (1)$$

where n represents the number of electrons transferred for each product formation, F is the Faraday constant (96,485 C·mol^{-1}), and Q represents the charge passed during FOR.

2.5 DFT calculations

DFT-derived machine learning potentials (MLP) were performed to analyze the FOR mechanism on Ag and Ag/Ag_2O. Detailed information can be found in the Electronic Supplementary Material (ESM).

3 Results and discussion

A schematic illustration of the principle for the formation of Ag/Ag_2O NPs@NF from Ag_2O NPs@NF is depicted in Fig. 2(a). There are two reactions during the structural reconstruction process that cause Ag_2O to turn into Ag. First, when the potential is less than 1.2 V, Ag^+ undergoes an electroreduction process [20]. The reaction equation is Eq. (2):

$$Ag^+ + e^- = Ag \quad (2)$$

Second, as the following equation illustrates, Ag_2O can be converted to Ag by HCHO (Eq. (3)):

$$HCHO + 2Ag_2O \rightarrow H_2O + CO_2\uparrow + 4Ag\downarrow \quad (3)$$

Ag_2O will rapidly reduce to Ag at the reduction potential according to Eq. (2). It is known that metastable metal oxides will remain on the electrode surface during cathodic processes, even if the potential is greater than the standard reduction potential [30–33]. During FOR, the electrode is immersed in the HCHO solution, HCHO can reduce the metastable Ag_2O to Ag on the surface of Ag/Ag_2O NPs@NF according to Eq. (3). In this study, the Ag/Ag_2O NPs@NF is obtained by catalyzing the Ag_2O NPs@NF directly in 1.0 M KOH solution containing 0.6 M HCHO at the potential of 0.2 V for 10 min. The electrolysis *i*–*t* curve is illustrated in Fig. 2(b). A

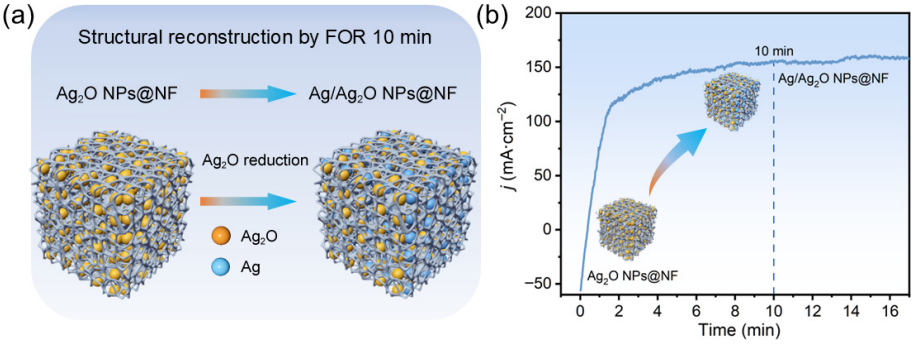

Figure 2 (a) Schematic diagram of the Ag/Ag_2O NPs@NF production principle derived from Ag_2O NPs@NF. (b) Chronoamperometric curve for the formation of Ag/Ag_2O by FOR electrolysis at 0.2 V.

gradual increase in the electrolysis current is observed as the electrolysis time prolongs. When the electrolysis time reaches 10 min, the current becomes stable, indicating that the Ag/Ag_2O NPs@NF has reached its optimal catalytic state.

The Ag/Ag_2O NPs@NF electrode in this work is covered with a Nafion membrane. Additionally, the reduction of metastable Ag_2O by HCHO can be postponed by nafion membrane. The LSV curves for FOR before and after coating a layer of Nafion membrane on the surface of the Ag plate were compared (Fig. S1(a) in the ESM). The FOR activity of the Ag plate decreases after coating with a Nafion membrane, indicating that the Nafion membrane on the electrode surface can impede the direct contact between HCHO and the electrode. We also carried out an additional experiment to confirm the Nafion membrane's efficacious effect on the Ag/Ag_2O NPs@NF. Ag_2O NPs should be completely reduced, including the metastable Ag_2O-oxide on the catalyst surface, by soaking them in HCHO solution for 12 h. Then prepare the electrode covered with Nafion membrane using the same method for preparing Ag/Ag_2O NPs@NF. The FOR performance of the HCHO-reduced Ag_2O NPs@NF is significantly worse than that of Ag/Ag_2O NPs@NF (Fig. S1(b) in the ESM). This indicates that the Nafion membrane coating plays a crucial role in the process of Ag_2O NPs@NF reconstruction into highly active Ag/Ag_2O NPs@NF. It is reported that Nafion membrane coating on the surface of the Pt plate can impede formic acid electrooxidation [34]. The Nafion membrane coating on the surface of catalyst can impede the contact of organic small molecules with the electrode, like formic acid or methanol [35, 36]. Similarly, the catalyst containing Ag-oxide with a Nafion membrane coating can also impede the reduction of Ag-oxide by HCHO. Additionally, during the reconstruction process, HCHO reaching the electrode surface will be decomposed to formate and H_2 by FOR, thereby minimizing the reduction effect of HCHO on Ag_2O. A comparative study on FOR's impact on the Ag/Ag_2O heterojunction structure was also carried out. The Ag/Ag_2O NPs@NF electrode's FOR potential increased from 0.16 to 0.25 V after being immersed for 24 h in a 1.0 M KOH solution containing 0.6 M HCHO, suggesting that FOR is also involved in preserving the Ag/Ag_2O heterojunction. In order to maintain electrode activity, the Ag/Ag_2O NPs@NF should not be immersed in HCHO solution for an extended period of time without electrolysis.

SEM images of Ag/Ag_2O NPs@NF are presented in Figs. 3(a) and 3(c). It is evident that the Ag_2O NPs have irregular particle shapes and are typically larger than 500 nm in size. The elemental distribution mappings of Ag/Ag_2O NPs@NF is presented in Fig. 3(b). It is evident that the elements F and S also showed up in addition to the elements Ag, Ni, and O. The Nafion membrane covering provides the components F and S. Figure 3(d) shows the TEM image of the Ag/Ag_2O NPs that were removed by ultrasonic treatment from the Ag/Ag_2O NPs@NF electrode. It can be seen that the Ag/Ag_2O NPs covered with uneven Nafion membrane. The high-resolution TEM (HRTEM) image of the Ag/Ag_2O NPs is presented in Fig. 3(e). The lattice fringes of d = 0.272, 0.204 and 0.236 nm, attributed to the (111) crystal plane of Ag_2O, (200) and (111) crystal planes of Ag. The HRTEM results indicated the presence of Ag/Ag_2O heterojunction on the catalyst surface. The XRD patterns of Ag_2O NPs, Ag NPs and Ag/Ag_2O NPs@NF are displayed in Fig. 3(f). Three conspicuous diffraction peaks at 32.8°, 38.0° and 54.9°, are exhibited by Ag_2O NPs completely coinciding with the (111), (200) and (220) planes of the PDF #41-1104 standard card of Ag_2O. Ag NPs displays four obvious diffraction peaks at 38.0°, 44.2°, 64.4°, and 77.4°, completely matching with (111), (200), (220) and (311) planes of the PDF #04-0783 standard

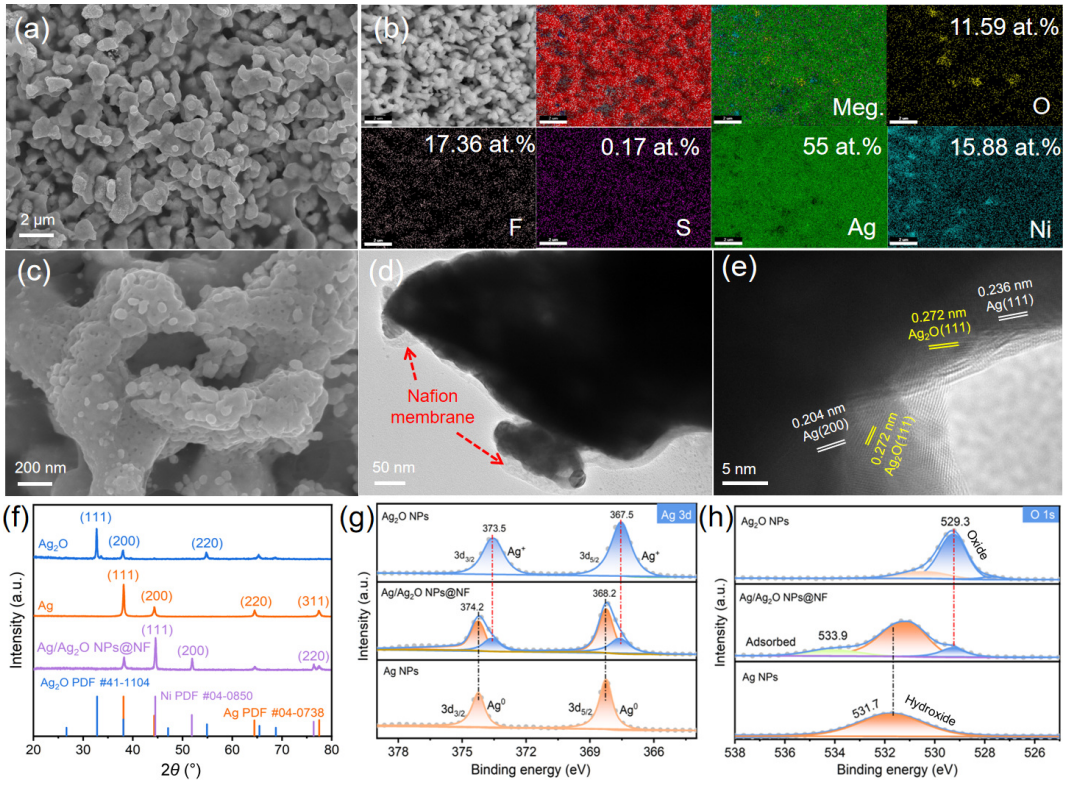

Figure 3 (a) and (c) SEM images, (b) elemental distribution mappings, (d) TEM image and (e) HRTEM image of Ag/Ag_2O NPs@NF. (f) XRD patterns of Ag_2O NPs, Ag NPs and Ag/Ag_2O NPs@NF. (g) and (h) Ag 3d and O 1s XPS spectra of Ag_2O NPs, Ag/Ag_2O NPs@NF and Ag NPs.

card for Ag. For the Ag/Ag_2O, it can be seen that except for the peak of NF, the rest of the peaks belong to Ag (PDF #04-0783). For the Ag/Ag_2O NPs@NF, most of the Ag_2O has already been reduced under the combined action of reduction potential and HCHO molecules, and the metastable oxide layer on the catalyst surface can remain stable even at the reduction potential. Since there is a very tiny amount of metastable Ag_2O on the surface of the Ag/Ag_2O NPs@NF, it is not visible in XRD. The detection depth of XRD is significantly greater than that of XPS. The presence of Ag_2O on the catalyst surface can be observed from XPS. Similar situations have also been reported in the literature [30].

To further investigate the morphology and structure of Ag/Ag_2O, the Ag 3d and O 1s XPS spectra of Ag_2O NPs, Ag/Ag_2O NPs@NF, and Ag NPs are shown in Figs. 3(d) and 3(g), respectively. The prominent peaks at 373.5 and 367.5 eV correspond to Ag^+ $3d_{3/2}$ and Ag^+ $3d_{5/2}$, respectively, while the strong peaks of Ag^0 at 374.2 and 368.2 eV are attributed to Ag^0 $3d_{3/2}$ and Ag0 $3d_{5/2}$, respectively [37]. Ag^0 and Ag^+ coexist in the prepared Ag/Ag_2O NFs@NF catalyst with the proportions of Ag^0 and Ag^+ about 30% and 70%, respectively. As shown in Fig. 3(h), the peaks at 531.7 and 533.9 eV correspond to the –OH and adsorbed O_2/H_2O, while the peak at 529.3 eV is characteristic of lattice O species [38]. The Ag/Ag_2O NPs@NF exhibit a significantly lower lattice O content than Ag_2O because Ag_2O can be reduced to Ag by HCHO in the solution.

LSV curves were measured for HCHO concentrations ranging from 0 to 1.0 M in 1.0 M KOH solution (Fig. S4(a) in the ESM). Ag/Ag_2O NPs@NF exhibited the best performance at 0.6 M, achieving the current density of 100 mA·cm^{-2} at a low potential of 0.16 V, outperforming the other concentrations of HCHO (Fig. S4(b) in the ESM). Therefore, all the subsequent electrochemical studies on HCHO oxidation were conducted using 1.0 M KOH and 0.6 M HCHO as the optimal electrolyte concentrations. The LSV curves of the prepared catalysts are depicted in Fig. 4(a) after 95% *iR* compensation. The Ag/Ag_2O NPs@NF catalyst demonstrated the lowest potential among the tested catalysts at the same current density, with FOR potentials of 0.1 V @ 50 mA·cm^{-2} and 0.16 V @ 100 mA·cm^{-2}. On the other hand, Ag NPs@NF and Ag plate required 0.33 and 0.45 V to achieve the current density of 50 while 0.46 and 0.53 V to reach 100 mA·cm^{-2}. The LSV results demonstrate that Ag/Ag_2O NPs@NF exhibits superior FOR performance. A comparison of the Ag/Ag_2O NPs@NF with the reported FOR catalysts is listed in Table S2 in the ESM. It can be seen that Ag/Ag_2O NPs@NF outperformed most of the other reported FOR electrocatalysts. Figure 4(b) shows impedance testing results reflecting the electron transfer rate of the catalysts. The Ag/Ag_2O NPs@NF catalyst displayed the smallest semicircle radius compared to Ag NPs@NF, Ag plate, and NF catalysts, indicating that the Ag/Ag_2O NPs@NF lowers charge transfer resistance, accelerates electron transfer rate, and improves the catalyst's activity. The stability of the Ag/Ag_2O NPs@NF catalyst was determined by chronoamperometry at a constant potential of 0.16 V with electrolyte renewal every hour for 5 cycles as illustrated in Fig. 4(c). The current drop for each cycle is mainly caused by the consumption of HCHO. The current value also recovers when the HCHO concentration in the electrolyte recovers, suggesting the catalyst's excellent chemical stability. Figure S10 in the ESM displays the Ag 3d XPS spectrum of Ag/Ag_2O NPs@NF following a 5-h electrolysis. The percentage of Ag^+ drops to 18% after the electrolysis period. This suggests that, with the barrier of Nafion membrane providing protection, Ag/Ag_2O heterojunction can persist steadily and retain high catalytic activity during the FOR process.

The catalyst's electrochemical stability is demonstrated by the nearly overlapping polarization curves before and after electrolysis

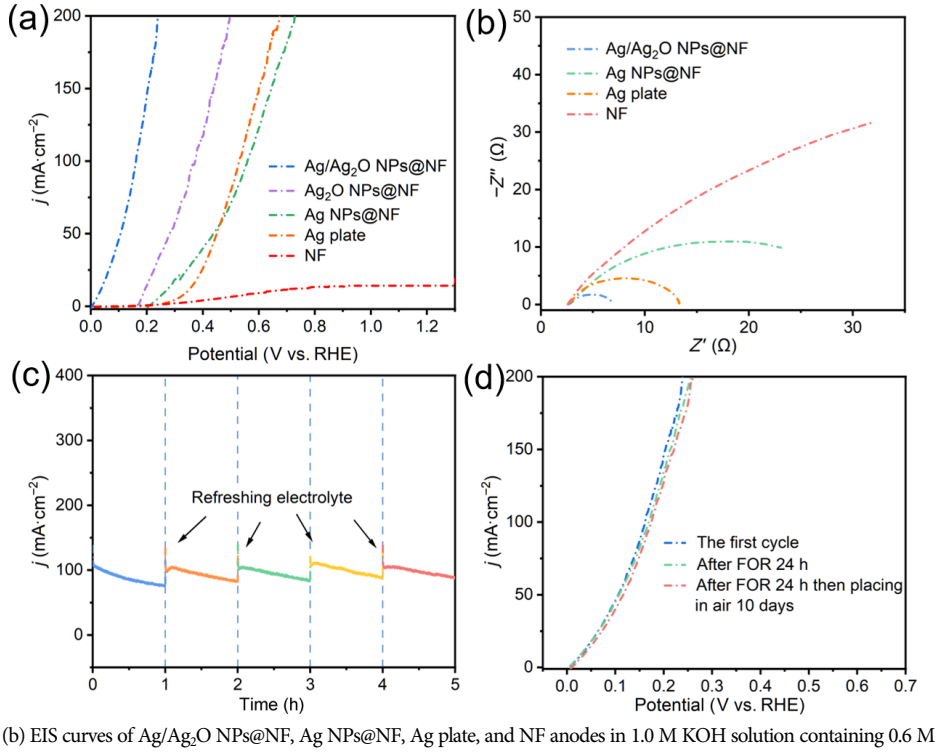

Figure 4 (a) LSV curves. (b) EIS curves of Ag/Ag_2O NPs@NF, Ag NPs@NF, Ag plate, and NF anodes in 1.0 M KOH solution containing 0.6 M HCHO. Note that Ag_2O cannot exist stably in the electrolyte due to the reducibility of HCHO. The LSV curve (first cycle) for Ag_2O NPs@NF cannot accurately reflect the catalytic ability of Ag_2O and is merely for reference. (c) Chronoamperometric curves at a potential of 0.16 V with the periodic replenishment of fresh HCHO back to its original 0.6 M concentration in the anolyte. (d) LSV curves before and after the *i*–*t* test.

for 24 h, as illustrated in Fig. 4(d). In addition, the Ag/Ag_2O NPs@NF electrode also exhibits the attribute of easy storage. The LSV curve of the Ag/Ag_2O NPs@NF electrode illustrated in Fig. 4(d) is nearly identical to the first cycle after being placed in the air for 10 days. At FOR's oxidation potential, the Ag/Ag_2O NPs@NF electrode retains its high catalytic activity.

The Cannizzaro reaction typically occurs in a strongly alkaline HCHO solution [39]. It is a side reaction of FOR with the reaction process and is represented as follows (Eq. (4)):

$$2HCHO + H_2O \rightarrow HCOOH + CH_3OH \quad (4)$$

At the same time, the commercially available 37% HCHO solution contains 10% CH_3OH as a stabilizer. Solid polyformaldehyde (18 $g \cdot L^{-1}$) was employed as the electrolyte due to the potential interference with product analysis [20]. The LSV curves of polyformaldehyde and formaldehyde solutions are almost identical (Fig. 5(a)) showing that polyformaldehyde can be used as an electrolyte to analyze the product while avoiding the interference of CH_3OH stabilizer. At a constant current density of 25 $mA \cdot cm^{-2}$ the gas produced by the anode and cathode was collected using the drainage method as illustrated in Fig. 5(b). The anode gas volume was 13 mL comparable to the volume of the cathode gas (13 mL). Gas chromatography was used to identify the collected gas (Fig. S6 in the ESM), indicating that the collected gas was pure H_2. The Faradaic efficiency of the produced H_2 by FOR at the anode can be calculated by the amount of collected gas. The liquid products were measured using ^1H NMR with t-butanol as the internal standard as illustrated in Fig. 5(c). The content standard curves of CH_3OH and formate measured by ^1H NMR are depicted in Fig. S7 in the ESM. The amount produced by the Cannizzaro reaction needs to be subtracted from the same amount of CH_3OH and the formate generated by the Cannizzaro reaction is the same in the product. Therefore, the amount of formate produced by electrolysis can be obtained from which FE of formate produced through FOR can be calculated. Figure 5(d) depicts that the FEs for both formate and H_2 production are 100% (±3%). The volume data of H_2 produced by FOR with different current densities along with NMR data are illustrated in Table S1 in the ESM.

The spontaneous Cannizzaro reaction is an unavoidable side reaction during FOR that needs to be minimized as much as possible. The proportion of formate produced by electrolysis is only 40% at the current density of 150 $mA \cdot cm^{-2}$ (Fig. 5(c)). Due to the use of a large volume electrolyte (50 mL) during electrolysis, the proportion of formate generated by spontaneous reactions is high. We reduced the volume of electrolyte and used 8 mL electrolyte for electrolysis, which increased the proportion of formate generated by electrolysis to 72.5% (Fig. 5(d)). The proportion of spontaneous reactions can be reduced by reducing the volume of electrolyte. In industry, the proportion of spontaneous reactions can be reduced by using freshly prepared electrolytes and flowing electrolysis. In order to compare the amount of formate generated by spontaneous reaction and electrolysis at the same time, the electrolyte after electrolysis or left in air 30 min were detected by ^1H NMR as shown in Fig 5(d). It can be seen that the peak of formate after electrolysis for 30 min is obviously higher than the peak when it is left in air 30 min. It can be seen that the integral value of methanol after 30 min of spontaneous reaction is 0.17, and the integral value of methanol after electrolysis reaction is 0.20. Compared with the amount of methanol generated by spontaneous reaction, there is a little increase, which may be due to the disturbance of H_2 bubbles in the solution accelerating the spontaneous reaction.

It is reported that the lower the concentration of HCHO in 1.0 M KOH, the weaker the Cannizzaro reaction [3]. The ratio of formate produced through spontaneous reaction and electrolysis reaction is illustrated in Fig. S11 in the ESM. The findings show that the percentage of formate produced by electrolysis rises as HCHO concentration falls. At 0.1 M concentration of HCHO, the

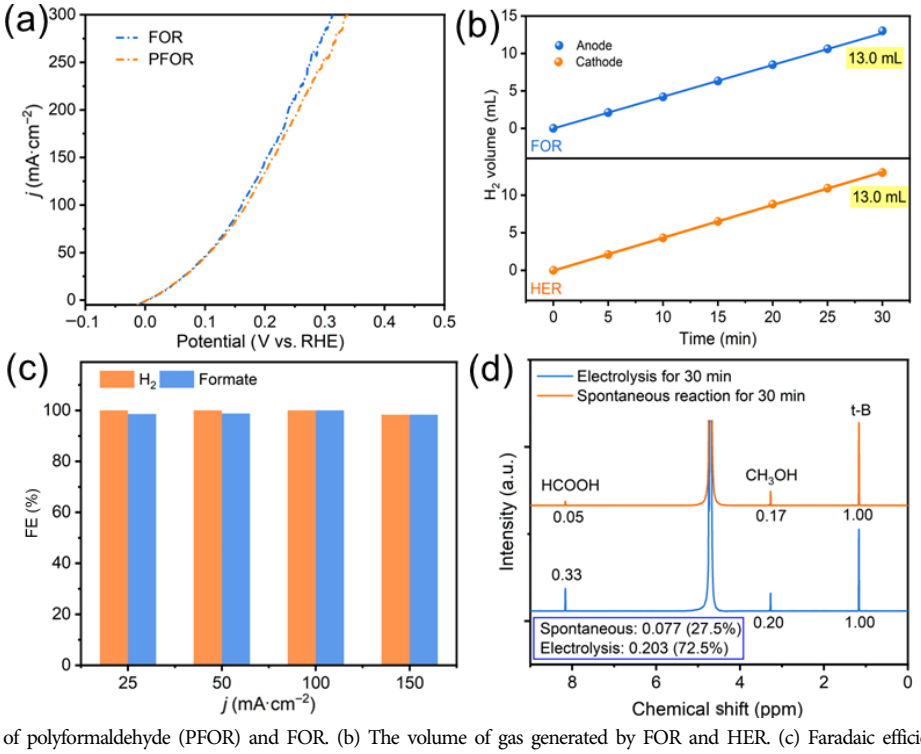

Figure 5 (a) LSV curves of polyformaldehyde (PFOR) and FOR. (b) The volume of gas generated by FOR and HER. (c) Faradaic efficiencies of H_2 and formate production at different current densities (see Table S1 in the ESM for details). (d) The ^1H NMR spectra of the electrolyte after electrolysis and left in air 30 min.

proportion of formate from FOR electrolysis can approach 85%. The incidence of spontaneous reactions can also be slowed down by lowering the concentration of HCHO in 1.0 M KOH.

We employed a first-principles-based approach to investigate the mechanism at the atomic scale. The performance test revealed that the Ag/Ag_2O catalyst exhibits better FOR activity than the Ag catalyst. To further understand the mechanism of catalysis, we employed MLP to construct the structures of the Ag_2O(111) surface, Ag(111) surface, and Ag–Ag_2O interface and utilized the computational hydrogen electrode (CHE) method to calculate their activities. Considering the complexity of the system and the presence of multiple sites, we constructed approximately 10 sites across different models (Fig. 6(a)) and selected the most active one as the actual catalytic site. Furthermore, during the construction of the reaction pathway, we also considered the adsorption and desorption of both HCHO and HCOOH. We found that the adsorption processes for almost all HCHO sites were endothermic (Fig. S14 in the ESM), which suggests that HCHO adsorption can be neglected. Instead, we considered the simultaneous protonation during HCHO adsorption, leading to the formation of $H_2C(OH)O^*$. For HCOOH*, however, a significant number of adsorption sites were exothermic (Fig. S15 in the ESM), necessitating site-specific analysis. The Gibbs adsorption-free energies for formate and H_2 production on two different models are calculated separately due to the presence of formate and H_2 products during the FOR process. The largest Gibbs energies (ΔG^0_{max}) of $H_2C(OH)O^*$ for producing formate on the Ag_2O surface, Ag surface and the Ag–Ag_2O interface models as depicted in Fig. 6(b) are −0.43, −0.51, and −0.55 eV, indicating better activity at the Ag–Ag_2O interface. Furthermore, the ΔG^0_{max} of HER on the Ag_2O surface, Ag surface, and the Ag–Ag_2O interface models are 0.89, 0.42, and 0.08 eV (Fig. 6(c)), further suggesting the superior activity at the Ag–Ag_2O interface. These results demonstrate that the Ag–Ag_2O interface exhibits better activity for both FOR and HER, highlighting the role of partial oxidation in activating the reaction. The results of theoretical analysis correspond well with the HER experimental data exhibiting overpotential of 0.46, 0.46, and 0.34 V at 100 mA·cm^{-2} for Ag_2O NPs, Ag NPs, and Ag/Ag_2O NPs, respectively. The DFT results suggested the poor catalytic performance of Ag_2O thereby not suitable as a FOR catalyst. In fact, Ag_2O cannot exist stably in the electrolyte due to the reducibility of HCHO, making it unable to serve as a stable FOR catalyst. The field emission desorption (FED) diagram indicates that partial oxidation enhances the adsorption strength and reactivity, thereby increasing the catalytic activity. The adsorption energies for the reaction intermediates $H_2C(OH)O^*$ and *H on Ag–Ag_2O interface are all stronger than that of Ag surface. Therefore, the excellent FOR performance of the Ag–Ag_2O interface can be mainly attributed to its strong adsorption ability of the intermediates (*H and $H_2C(OH)O^*$). The mechanistic model of Ag and Ag/Ag_2O towards FOR is shown in Fig. 6(e).

As depicted in Fig. 7(a), the FOR LSV curve of Ag/Ag_2O NPs@NF exhibits almost 0 onset potential with a very steep increase in anodic current density reaching 100 mA·cm^{-2} at only 0.16 V in 1.0 M KOH and 0.6 M HCHO. A higher potential (1.73 V) is required for Ag/Ag_2O NPs@NF as an OER electrocatalyst to achieve the same current density of 100 mA·cm^{-2}. The conversion of Ag^0 to Ag^+ requires a higher potential (> 1.2 V) than FOR, therefore Ag/Ag_2O can stably catalyze FOR exhibiting a large current and unaffected by its oxidation reaction. The *i*–*t* curves for Ag/Ag_2O NPs@NF under the continuous addition of 0.1 M CH_3OH, 0.1 M formate, and 0.1 M HCHO in 1.0 M KOH are displayed in Fig. 7(b). There is no change in the anodic current upon addition of formate at 0.2 V, suggesting that Ag/Ag_2O NPs@NF cannot catalyze the electrochemical oxidation of CH_3OH and formate at low potential. In contrast, the addition of 0.1 M HCHO immediately increases the anodic current to 30 mA·cm^{-2} indicating that Ag/Ag_2O NPs@NF catalyst exhibits good selectivity for FOR and is not affected by CH_3OH and formate. As shown in Fig. 7(c), HER||FOR is more beneficial than HER||OER. The

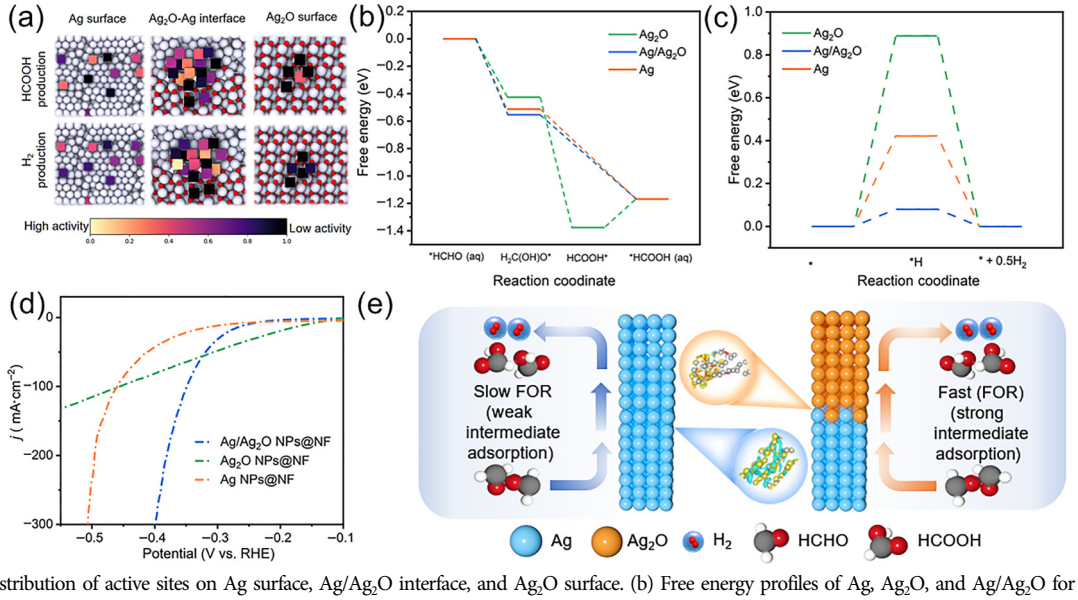

Figure 6 (a) Distribution of active sites on Ag surface, Ag/Ag_2O interface, and Ag_2O surface. (b) Free energy profiles of Ag, Ag_2O, and Ag/Ag_2O for FOR. Note that HCOOH adsorption on Ag is exothermic and should therefore be taken into account, whereas it is endothermic on Ag_2O and Ag/Ag_2O and can be disregarded. For all three surfaces, HCHO adsorption is endothermic, so it is not considered. (c) Free energy profiles of Ag, Ag_2O, and Ag/Ag_2O for HER. The applied potential is zero for both FOR and HER. (d) LSV curves of HER for Ag NPs@NF, Ag_2O NPs@NF, and Ag/Ag_2O@NF. Note that Ag_2O cannot exist stably in the electrolyte due to the reducibility of HCHO. The LSV curve (first cycle) for Ag_2O NPs@NF cannot accurately reflect the catalytic ability of Ag_2O and is merely for reference. (e) The mechanistic model of Ag and Ag/Ag_2O towards FOR.

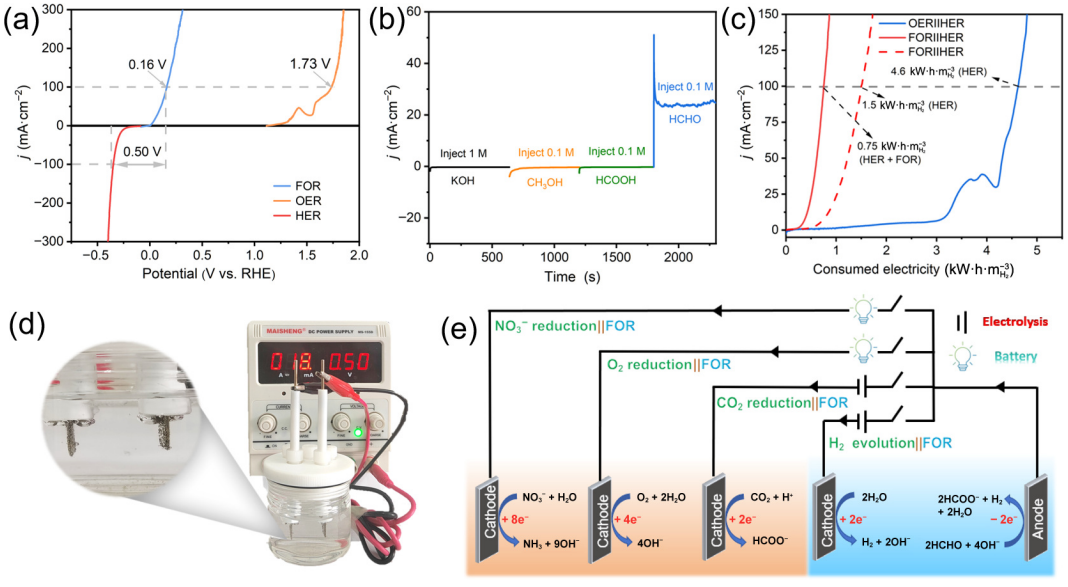

Figure 7 (a) LSV curves of Ag/Ag_2O NPs@NF for FOR in 1.0 M KOH with 0.6 M HCHO, and for HER and OER in 1.0 M KOH. (b) Chronoamperometric curve at a potential of 0.16 V in 1.0 M KOH with the continuous addition of 0.1 CH_3OH, 0.1 HCOOH, and 0.1 M HCHO. (c) Electricity consumed for H_2 production using Ag/Ag_2O NPs@NF as anode and cathode for FOR||HER and OER||HER. (d) The photo of low voltage electrolysis device. (e) Illustration of FOR coupled with other cathode reactions.

consumed electricity for HER||OER is 4.6 $kW{\cdot}h{\cdot}m_{H_2}^{-3}$ at the current density of 100 $mA{\cdot}cm^{-2}$, which is higher than that of HER||FOR (0.75 $kW{\cdot}h{\cdot}m_{H_2}^{-3}$). The cell potential of HER||FOR is only 0.5 V at the current density of 18 $mA{\cdot}cm^{-2}$ in a membrane-free single chamber electrolytic cell, with visible bubbles at the cathode and anode (Fig. 7(d)). This significant energy-saving advantage will enable FOR to be coupled with other valuable reduction reactions in addition to being used for H_2 production from water. For example, it can be employed to couple with CO_2 reduction to formate, with the reduction reaction of nitric acid to NH_3 to form a battery, and coupling with oxygen reduction reactions for direct HCHO fuel cell [26, 27, 39, 40]. FOR coupling with other cathode reactions is shown in Fig. 7(e). FOR will have broad prospects in the field of energy electrocatalysis owing to its great advantages.

FOR is an electrochemical synthesis reaction, which can be coupled with HER for H_2 production. However, coupling FOR only for the production of H_2 is not cost-effective owing to the low molar mass of H_2. The saved electricity cost is insufficient to offset the cost of formaldehyde raw materials. Therefore, utilization of the FOR products is inevitable. It is known that the FOR in KOH solution produces HCOOK, which can be obtained by distillation. However, the HCOOK is low value-added product and its market is small. Potassium diformate (KDF) with higher added value can be obtained by the addition of more HCOOH to the electrolytic product. The schematic operating units of the integrated process for HER||FOR to produce KDF, H_2, and CH_3OH are shown in Fig. 8(a). Since the addition of antibiotics to animal feed is prohibited, KDF is a new and safe growth stimulant for animals [41]. It has been demonstrated that supplementing pigs' diets with KDF enhances growth performance, lowers the amount of E. coli and Salmonella in the intestines, and avoids diarrhea [42]. KDF is a high-value feed additive that is safe and in high demand in the breeding sector. The white KDF crystal was obtained and confirmed by Fourier transformation infrared (FT-IR) spectrum and compared with commercial KDF in Fig. 8(b).

4 Conclusions

In summary, the ultra-low potential FOR catalyst of Ag/Ag_2O NPs@NF with high current density and high stability has been prepared in this study. The FOR potential to achieve the current density of 100 $mA{\cdot}cm^{-2}$ on the Ag/Ag_2O NPs@NF electrode was only 0.16 V, significantly lower than its OER potential (1.73 V). The Faradaic efficiencies for producing formate and H_2 from FOR both

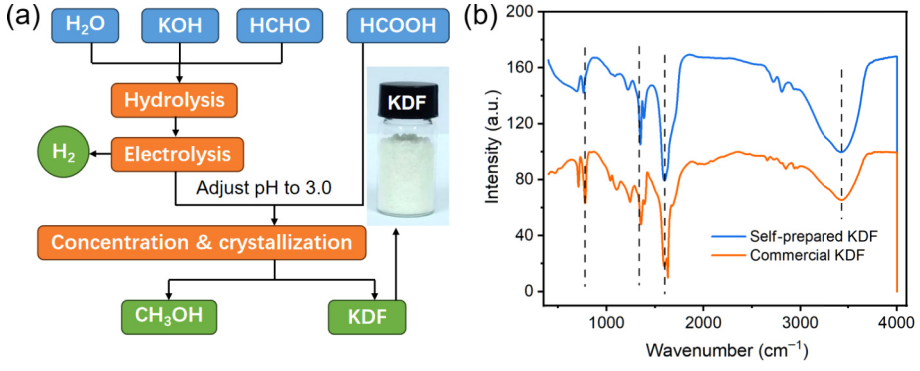

Figure 8 (a) Schematic operating units of the integrated process for HER||FOR to produce potassium diformate, H_2, and CH_3OH. (b) FT-IR spectra of self-prepared and commercial KDF.

reached 100%. When the Ag/Ag_2O NPs@NF were employed both as anode and cathode, the electricity consumed at the current density of 100 mA·cm^{-2} for HER||FOR was only 0.75 kW·h·$m_{H_2}^{-3}$, significantly lower than that of HER||OER (4.6 kW·h·$m_{H_2}^{-3}$). The DFT results demonstrated that the activity on the Ag–Ag_2O interface is better than that of Ag for both FOR and HER, highlighting the role of partial oxidation of Ag in activating the reaction. The Ag/Ag_2O NPs@NF prepared in this work has the characteristics of low cost, high activity, easy synthesis, and easy storage, which is expected to be industrially applied for H_2 production.

Electronic Supplementary Material: Supplementary material (details of theoretical calculation process, Figs. S1–S15, and Tables S1 and S2) is available in the online version of this article at https://doi.org/10.26599/NR.2025.94907110.

Data availability

All data needed to support the conclusions in the paper are presented in the manuscript and the ESM. Additional data related to this paper may be requested from the corresponding author upon request.

Acknowledgements

The work was supported by the National Natural Science Foundation of China (Nos. 22176166 and 22179034) and the Natural Science Foundation of Heilongjiang Province (No. ZD2023B002).

Declaration of competing interest

All the contributing authors report no conflict of interests in this work.

Author contribution statement

H. T. S.: Investigation, data curation, software, writing – original draft, formal analysis. R. Z.: Conceptualization, supervision, formal analysis, validation, methodology, writing – original draft, writing – review & editing. C. C. W.: Investigation, software. X. P. K.: Software. L. L. P.: Investigation, writing – original draft. M. J. W.: visualization. W. W.: Project administration, funding acquisition. W. X. L.: Conceptualization, formal analysis, resources, writing – review & editing, supervision. L. W.: Supervision, project administration, funding acquisition, writing – review & editing.

Use of AI statement

None.

References

[1] Xie, H. P.; Zhao, Z. Y.; Liu, T.; Wu, Y. F.; Lan, C.; Jiang, W. C.; Zhu, L. Y.; Wang, Y. P.; Yang, D. S.; Shao, Z. P. A membrane-based seawater electrolyser for hydrogen generation. *Nature* **2022**, *612*, 673–678.

[2] Li, Y.; Han, J.; Bao, W. W.; Zhang, J. J.; Ai, T. T.; Yang, M. M.; Yang, C. M.; Zhang, P. F. Self-derivation and reconstruction of silver nanoparticle reinforced cobalt-nickel bimetallic hydroxides through interface engineering for overall water splitting. *J. Energy Chem.* **2024**, *90*, 590–599.

[3] Yu, H. J.; Jiang, S. J.; Zhan, W. J.; Liang, Y. Q.; Deng, K.; Wang, Z. Q.; Xu, Y.; Wang, H. J.; Wang, L. Formaldehyde oxidation boosts ultra-low cell voltage industrial current density water electrolysis for dual hydrogen production. *Chem. Eng. J.* **2023**, *475*, 146210.

[4] Wu, Z. Y.; Chen, F. Y.; Li, B. Y.; Yu, S. W.; Finfrock, Y. Z.; Meira, D. M.; Yan, Q. Q.; Zhu, P.; Chen, M. X.; Song, T. W. et al. Non-iridium-based electrocatalyst for durable acidic oxygen evolution reaction in proton exchange membrane water electrolysis. *Nat. Mater.* **2023**, *22*, 100–108.

[5] Zhong, C. Z.; Zhang, J. X.; Zhang, L. H.; Tu, Y. H.; Song, H. Y.; Du, L.; Cui, Z. M. Composition-tunable $Co_{3-x}Fe_xMo_3N$ electrocatalysts for the oxygen evolution reaction. *ACS Energy Lett.* **2023**, *8*, 1455–1462.

[6] Zhang, R.; Zhu, L.; Lv, W. X.; Wei, M. J.; Wang, L.; Wang, W. Facile synthesis of Ni_3S_2 nanosheets with abundant active sites induced by Fe incorporation on Ni foam for enhanced oxygen evolution reaction. *Appl. Surf. Sci.* **2023**, *610*, 155537.

[7] Lv, W. X.; Zhu, L.; Kong, X. P.; Shi, H. T.; Wang, C. C.; Zhang, R.; Wang, W. Enhancement effects of Fe-doped Ni_3S_2 on efficient electrochemical urea oxidation and mechanism insights. *J. Alloys Compd.* **2023**, *965*, 171292.

[8] Yang, M.; Li, Y. Y.; Dong, C. L.; Li, S. K.; Xu, L. T.; Chen, W.; Wu, J. C.; Lu, Y. X.; Pan, Y. P.; Wu, Y. D. et al. Correlating the valence state with the adsorption behavior of a Cu-based electrocatalyst for furfural oxidation with anodic hydrogen production reaction. *Adv. Mater.* **2023**, *35*, 2304203.

[9] Wang, Y.; Xia, S.; Cai, R.; Zhang, J. F.; Yu, C. P.; Cui, J. W.; Zhang, Y.; Wu, J. J.; Wu, Y. C. Dynamic reconstruction of two-dimensional defective Bi nanosheets for efficient electrocatalytic urea synthesis. *Angew. Chem., Int. Ed.* **2024**, *63*, e202318589.

[10] Wu, X. H.; Wang, Y.; Wu, Z. S. Design principle of electrocatalysts for the electrooxidation of organics. *Chem* **2022**, *8*, 2594–2629.

[11] Luo, F.; Pan, S. Y.; Xie, Y. H.; Li, C.; Yu, Y. J.; Yang, Z. H. Atomically dispersed Ni electrocatalyst for superior urea-assisted water splitting. *J. Energy Chem.* **2024**, *90*, 1–6.

[12] Chen, R. Z.; Yang, Y. K.; Wu, W.; Chen, S. H.; Wang, Z. C.; Zhu, Y.; Cheng, N. C. Reconstructed β-NiOOH enabling highly efficient and ultrastable oxygen evolution at large current density. *Chem. Eng. J.* **2024**, *480*, 148100.

[13] Zhao, L.; Lv, Z.; Shi, Y.; Zhou, S. L.; Liu, Y.; Han, J. N.; Zhang, Q.; Lai, J. P.; Wang, L. Simultaneous generation of furfuryl alcohol, formate, and H_2 by co-electrolysis of furfuryl and HCHO over bifunctional CuAg bimetallic electrocatalysts at ultra-low voltage. *Energy Environ. Sci.* **2024**, *17*, 770–779.

[14] Ji, K. Y.; Xu, M.; Xu, S. M.; Wang, Y.; Ge, R. X.; Hu, X. Y.; Sun, X. M.; Duan, H. H. Electrocatalytic hydrogenation of 5-hydroxymethylfurfural promoted by a Ru_1Cu single-atom alloy catalyst. *Angew. Chem., Int. Ed.* **2022**, *61*, e202209849.

[15] Zhu, Y. Q.; Zhou, H.; Dong, J. C.; Xu, S. M.; Xu, M.; Zheng, L. R.; Xu, Q.; Ma, L. N.; Li, Z. H.; Shao, M. F. et al. Identification of active sites formed on cobalt oxyhydroxide in glucose electrooxidation. *Angew. Chem., Int. Ed.* **2023**, *62*, e202219048.

[16] Yi, Y. N.; Li, J. S.; Cui, C. H. Trimetallic FeCoNi disulfide nanosheets for CO_2-emission-free methanol conversion. *Chin. Chem. Lett.* **2022**, *33*, 1006–1010.

[17] Chen, J. H.; Ahmad, M.; Zhang, Y.; Ye, H. Q.; Wang, L.; Zhang, J. J.; Fu, X. Z.; Luo, J. L. Versatile Mo modulation effects enable efficient electrocatalytic aqueous methanol electro-reforming over surface-engineered NiCoMo alloy. *Chem. Eng. J.* **2023**, *454*, 140056.

[18] Lestarini, D. T.; Hong, J. W. Intermetallic Pd_3Pb nanobranches with low-coordinated surface atoms for highly efficient ethanol oxidation reaction. *Appl. Surf. Sci.* **2023**, *610*, 155311.

[19] Wang, X. H.; Zhang, Z. N.; Wang, Z.; Ding, Y.; Zhai, Q. G.; Jiang, Y. C.; Li, S. N.; Chen, Y. Ultra-thin $CoNi_{0.2}P$ nanosheets for plastics and biomass participated hybrid water electrolysis. *Chem. Eng. J.* **2023**, *465*, 142938.

[20] Han, G. Q.; Li, G. D.; Sun, Y. J. Electrocatalytic dual hydrogenation of organic substrates with a Faradaic efficiency approaching 200%. *Nat. Catal.* **2023**, *6*, 224–233.
[21] Li, S. L.; Liu, D. M.; Wang, G. W.; Ma, P. J.; Wang, X. L.; Wang, J. C.; Ma, R. G. Vertical 3D nanostructures boost efficient hydrogen production coupled with glycerol oxidation under alkaline conditions. *Nano-Micro Lett.* **2023**, *15*, 189.
[22] Yang, Y. Y.; Zou, R.; Gan, J. Y.; Wei, Y. J.; Chen, Z. X.; Li, X. H.; Admassie, S.; Liu, Y. P.; Peng, X. W. Integrating electrocatalytic seawater splitting and biomass upgrading via bifunctional nickel cobalt phosphide nanorods. *Green Chem.* **2023**, *25*, 4104–4112.
[23] Wu, K. L.; Cao, C. Y.; Li, K. R.; Lyu, C. J.; Cheng, J. R.; Li, H. Y.; Hu, P. F.; Wu, J. W.; Lau, W. M.; Zhu, X. X. et al. Regulating electronic structure by Mn doping for nickel cobalt hydroxide nanosheets/carbon nanotube to promote oxygen evolution reaction and oxidation of urea and hydrazine. *Chem. Eng. J.* **2023**, *452*, 139527.
[24] Wang, T. H.; Tao, L.; Zhu, X. R.; Chen, C.; Chen, W.; Du, S. Q.; Zhou, Y. Y.; Zhou, B.; Wang, D. D.; Xie, C. et al. Combined anodic and cathodic hydrogen production from aldehyde oxidation and hydrogen evolution reaction. *Nat. Catal.* **2022**, *5*, 66–73.
[25] Li, G. D.; Han, G. Q.; Wang, L.; Cui, X. Y.; Moehring, N. K.; Kidambi, P. R.; Jiang, D. E.; Sun, Y. J. Dual hydrogen production from electrocatalytic water reduction coupled with formaldehyde oxidation via a copper-silver electrocatalyst. *Nat. Commun.* **2023**, *14*, 525.
[26] Xiao, L.; Dai, W. D.; Mou, S. Y.; Wang, X. Y.; Cheng, Q.; Dong, F. Coupling electrocatalytic cathodic nitrate reduction with anodic formaldehyde oxidation at ultra-low potential over Cu_2O. *Energy Environ. Sci.* **2023**, *16*, 2696–2704.
[27] Li, M. Y.; Wang, T. H.; Zhao, W. X.; Wang, S. Y.; Zou, Y. Q. A pair-electrosynthesis for formate at ultra-low voltage via coupling of CO_2 reduction and formaldehyde oxidation. *Nano-Micro Lett.* **2022**, *14*, 211.
[28] Pan, Y. P.; Li, Y. Y.; Dong, C. L.; Huang, Y. C.; Wu, J. C.; Shi, J. Q.; Lu, Y. X.; Yang, M.; Wang, S. Y.; Zou, Y. Q. Unveiling the synergistic effect of multi-valence Cu species to promote formaldehyde oxidation for anodic hydrogen production. *Chem* **2023**, *9*, 963–977.
[29] Wang, P.; Zheng, J.; Xu, X.; Zhang, Y. Q.; Shi, Q. F.; Wan, Y.; Ramakrishna, S.; Zhang, J.; Zhu, L. Y.; Yokoshima, T. et al. Unlocking efficient hydrogen production: Nucleophilic oxidation reactions coupled with water splitting. *Adv. Mater.* **2024**, *36*, 2404806.
[30] Chen, Y. H.; Kanan, M. W. Tin oxide dependence of the CO_2 reduction efficiency on tin electrodes and enhanced activity for tin/tin oxide thin-film catalysts. *J. Am. Chem. Soc.* **2012**, *134*, 1986–1989.
[31] Baruch, M. F.; Pander III, J. E.; White, J. L.; Bocarsly, A. B. Mechanistic insights into the reduction of CO_2 on tin electrodes using *in situ* ATR-IR spectroscopy. *ACS Catal.* **2015**, *5*, 3148–3156.
[32] Lv, W. X.; Zhou, J.; Bei, J. J.; Zhang, R.; Wang, L.; Xu, Q.; Wang, W. Electrodeposition of nano-sized bismuth on copper foil as electrocatalyst for reduction of CO_2 to formate. *Appl. Surf. Sci.* **2017**, *393*, 191–196.
[33] Zhang, R.; Lv, W. X.; Lei, L. X. Role of the oxide layer on Sn electrode in electrochemical reduction of CO_2 to formate. *Appl. Surf. Sci.* **2015**, *356*, 24–29.
[34] Zhang, R.; Lv, W. X.; Li, G. H.; Mezaal, M. A.; Li, X. J.; Lei, L. X. Retarding of electrochemical oxidation of formate on the platinum anode by a coat of Nafion membrane. *J. Power Sources* **2014**, *272*, 303–310.
[35] Rejal, S. Z.; Masdar, M. S.; Kamarudin, S. K. A parametric study of the direct formic acid fuel cell (DFAFC) performance and fuel crossover. *Int. J. Hydrogen Energy* **2014**, *39*, 10267–10274.
[36] Rhee, Y. W.; Ha, S. Y.; Masel, R. I. Crossover of formic acid through Nafion® membranes. *J. Power Sources* **2003**, *117*, 35–38.
[37] Sugianto Prabowo Rahardjo, S.; Shih, Y. J. *In-situ* phase transformation of silver oxide nanoparticles encapsulated in reduced graphene oxide (Ag/rGO) for direct electrochemical ammonia oxidation. *Chem. Eng. J.* **2023**, *473*, 145396.
[38] Cheng, L. Z.; Zhang, R.; Lv, W. X.; Shao, L. Y.; Wang, Z.; Wang, W. Surface phosphation of 3D $NiCo_2O_4$ nanowires grown on Ni foam as an efficient bifunctional catalyst for water splitting. *Nano* **2020**, *15*, 2050024.
[39] Yang, Y.; Wu, X. X.; Ahmad, M.; Si, F. Z.; Chen, S. J.; Liu, C. H.; Zhang, Y.; Wang, L.; Zhang, J. J.; Luo, J. L. et al. A direct formaldehyde fuel cell for CO_2-emission free co-generation of electrical energy and valuable chemical/hydrogen. *Angew. Chem., Int. Ed.* **2023**, *62*, e202302950.
[40] An, S. Y.; Zhao, Z. H.; Bu, J.; He, J. X.; Ma, W. X.; Lin, J.; Bai, R.; Shang, L.; Zhang, J. Multi-functional formaldehyde-nitrate batteries for wastewater refining, electricity generation, and production of ammonia and formate. *Angew. Chem., Int. Ed.* **2024**, *63*, e202318989.
[41] Zhou, H.; Ren, Y.; Li, Z. H.; Xu, M.; Wang, Y.; Ge, R. X.; Kong, X. G.; Zheng, L. R.; Duan, H. H. Electrocatalytic upcycling of polyethylene terephthalate to commodity chemicals and H_2 fuel. *Nat. Commun.* **2021**, *12*, 4679.
[42] Lin, Y.; Zhai, J. L.; Wang, Y. T.; Guo, P. T.; Zhang, J.; Wang, C. K.; Jin, L.; Gao, Y. Y. Potassium diformate alleviated inflammation of IPEC-J2 cells infected with EHEC. *Vet. Microbiol.* **2024**, *291*, 110013.